

Observing 3-hydroxyanthranilate-3,4-dioxygenase in action through a crystalline lens

Yifan Wang^{¶,‡}, Kathy Fange Liu^{†,‡}, Yu Yang[¶], Ian Davis[¶], and Aimin Liu^{¶,*}

[¶]Department of Chemistry, University of Texas at San Antonio, San Antonio, TX 78249, USA

[†]Department of Biochemistry and Biophysics, Perelman School of Medicine, University of Pennsylvania, Philadelphia, PA 19104, USA

[‡]These authors contributed equally to this work.

*Correspondence to: Aimin Liu, E-mail: Feradical@utsa.edu

Table of Content

Supporting video	2
Materials and Method	2
Table S1. X-ray crystallography data collection and refinement statistics	7
Table S2. Coordination distances between exogenous ligands and iron before O ₂ activation.....	9
Table S3. Coordination distances between exogenous ligands and iron after O ₂ activation.....	10
Table S4. Occupancies of exogenous ligands after oxygen activation	11
Fig. S1. The fate of the HAO reaction product, ACMS, and biosynthesis of NAD ⁺	12
Fig. S2. Proposed thirty-two possible enol and enamine conformations of ACMS	13
Fig. S3. Density maps for the superoxo intermediate refined using different models	14
Fig. S4. Alignment of the captured superoxo with the published analogue structures.....	15
Fig. S5. Density maps for the alkylperoxo intermediate refined using various models	16
Fig. S6. Density maps for the ε-lactone intermediate refined using various models.....	17
Fig. S7. Additional views of the ε-lactone intermediate.	18
Fig. S8. Density maps for the monodentate product complex refined using various models	19
Fig. S9. Density maps for the bidentate product refined using various models.....	20
References	21

Supporting video

A 96-second video clip shows the transition from the substrate-free HAO to the catalytic intermediates determined in this work. The video clip is presented at the PNAS web site in mp4 format at 30 frames/s frame rate and 720p resolution (1280×720 pixels). The video was constructed using UCSF ChimeraX software (1).

Materials and Method

Materials—3-hydroxyanthranilic acid, ammonium iron(II) sulfate, ascorbate, magnesium chloride, Tris-HCl, DTT, and glycerol were the highest grades purchased from Sigma-Aldrich and used without further purification. 50% PEG 8000 solution was obtained from Hampton Research.

Expression and purification—HAO from *Cupriavidus metallidurans* was overexpressed in *Escherichia coli* (DE3) cells (Merck) and purified by nickel affinity chromatography as previously described (2, 3). Purified protein was reconstituted with five equivalents of $\text{NH}_4\text{Fe}(\text{SO}_4)_2$ anaerobically. The resultant protein then underwent size exclusion chromatography on a Superdex 200 (GE Healthcare) column, which was equilibrated with Tris-HCl buffer (10 mM, pH 7.6) containing 1 mM DTT. O_2 -production using chlorite dismutase followed the reported method (4).

Enzyme activity assays—The electronic absorption spectrum of HAO is essentially featureless above 280 nm. The anaerobic enzyme-substrate complex exhibits an absorption spectrum with a strong band at 325 nm due to the bound substrate. The ring-opened reaction product (ACMS) is pale yellow with absorption bands at 220, 270, and 360 nm. However, this species is unstable and cyclizes to QUIN, which exhibits a strong absorption band at 215 nm and a weak feature at 267 nm. These spectral differences allowed a previous study measuring the catalytic turnover at 25 s^{-1} ($K_m(3\text{-HAA})$ 22.4 μM) for the wild-type enzyme in solution at pH 7.2 (5). The transient kinetic data obtained by stopped-flow UV-vis spectroscopy in this work showed no evidence of the accumulation of any reactive intermediate (Figure 1B).

Kinetic Analysis—In the solution state, the time course of ACMS formation was obtained by monitoring absorbance at 360 nm using an Applied Photophysics (Leatherhead, UK) SX20 stopped-flow spectrometer equipped with a photodiode array detector as described previously (6). Data were fitted with a double exponential function.

$$Y = A_1 \cdot \exp(-\lambda_1 t) + A_2 \cdot \exp(-\lambda_2 t) + C.$$

The resulting parameters were:

$$\begin{aligned} A_1 &= -0.2130 \pm 0.0002; \lambda_1 = 38.87 \pm 0.05; \\ A_2 &= -0.4308 \pm 0.0001; \lambda_2 = 5.073 \pm 0.011; \\ C &= 0.8522 \pm 0.0004; R^2 = 1.000; \end{aligned}$$

Global analysis using a biphasic sequential reaction model was not necessary to fit the data, and no spectral features indicative of an intermediate could be found in the difference spectra. Two

summed exponential fit is most likely caused by heterogeneity among the iron centers of dimeric HAO.

HPLC analyses—A Thermo Scientific Ultimate-3000SD HPLC rapid separation system equipped with a photodiode array detector and an InertSustain C18 column (5 μ m particle size, 4.6 \times 100 mm, GL Sciences Inc.) was used for HPLC analyses. The sample injection volume was 10 μ L. The UV–vis spectra were recorded at full range with an online diode-array detector from 190 to 800 nm. The separation solvent was composed of 2% acetonitrile, 0.1 % formic acid, and 98% water. The HPLC profiles are presented with absorbance at 265 nm. QUIN and 3-HAA standards were purchased from Sigma with the highest purity. Standard samples were prepared by dissolving 3-HAA and QUIN in mother liquor with 20% glycerol to a final concentration of 5 mM and 0.5 mM, respectively. After removing the crystals by centrifugation, the reaction mixture was filtered using a 10-kDa molecular weight cutoff centrifugal filter unit (Millipore) prior to injection to the HPLC.

Product analysis by high-resolution MS—Mass spectra were collected on a maXis plus quadrupole time of flight mass spectrometer equipped with an electrospray ionization source (Bruker Daltonics) and operated in positive ionization mode. Samples were introduced via a syringe pump at a constant flow rate of 3 μ L/min. Instrumental parameters used were standard preset values for small molecules. Essential parameters are summarized as follows: capillary voltage, 3500 V with a set endplate offset of 500 V; nebulizer gas pressure, 0.4 bar; dry gas flow rate, 4.0 L/min; source temperature, 200 $^{\circ}$ C; quadrupole ion energy, 3.0 eV; collision energy, 5.0 eV as previously described for characterization of a heme iron-based enzymatic reaction (7). Scans were collected at a rate of one scan per second in the range of $50 \leq m/z \leq 1500$, and 60 s of data were averaged to yield a final spectrum. Compass Data Analysis software version 4.3 (Bruker Daltonics) was used to process all mass spectra.

Crystallization—Full length (1 – 174 amino acids) HAO with N-terminal tag was crystallized with conditions similar to those previously established (5) using hanging or sitting drop vapor diffusion in crystallization plates (Hampton Research). Single crystals suitable for X-ray data collection were obtained from drops assembled with 1 μ L of 20 mg/mL protein solution layered with 1 μ L reservoir solution containing 0.1 M Tris-HCl pH 8.5, 0.2 M $MgCl_2$, 1 mM DTT, 18% PEG 8000. The crystallization trays were set up in an anaerobic chamber (Coy Laboratory Products, MI, USA) maintained at or below 2 ppm O_2 . The trays were sealed and moved to a vibration-free, 16 $^{\circ}$ C crystallization incubator (Molecular Dimensions, Altamonte Springs, FL, USA). Crystals appeared within 24 h and were harvested when they were typically around 30 \times 50 \times 75 μ m in size.

X-ray data collection and structure refinement—X-ray diffraction data were collected at the beamlines SER-CAT section 19 and 22 of APS, and the beamline station 9-2 of SSRL. All data collections were performed at 100 K. The diffraction data were indexed, integrated, and scaled with HKL-2000 (8). These crystals are of the space group $P6_522$ with one protomer in the asymmetric unit that interacts with a protomer in a neighboring asymmetric unit to form the homodimer. Datasets (6VI5, 6VI6, 6VI7, 6VI8, and 6VIB) with severe anisotropy were truncated using the UCLA Diffraction Anisotropy Server (9). The structures were solved by molecular replacement using PHENIX (10) program with holo-HAO (PDB code 1YFU) as the search model.

Electron density was fitted and refined using PHENIX (10). Once the ligand identity was clear, the geometry restraints to metal centers were applied in refinement to result in reasonable coordination. Refinement results shown in the validation report from RCSB PDB, generated by EDS (REFMAC) that did not include specific restraints, may yield a discrepancy in electron density maps.

In the resting enzyme (Figure 3A), we observed extra electron density at the catalytic iron center that can be accommodated by two water molecules. Strong spherical density is observed in the pocket created by residues Val41, Arg47, Pro97, and Arg99 at the bottom of the substrate-binding cleft, which was assigned to a chloride anion. The presence of the Cl⁻ is a signature of the HAO resting state, and its presence and occupancy are linked to substrate binding because it must dissociate when 3-HAA binds. The electron density for the loops in the resting state fits the open conformation well, but not the closed conformation (Figure 3D).

Two distinct substrate-bound HAO structures (Figure 3, panels B and C) were obtained under anaerobic conditions by soaking crystals in mother liquor with 1 mM 3-HAA. In the first transient E•S complex, when 3-HAA was modeled, refinement yielded $2F_{\text{obs}}-F_{\text{calc}}$ and $F_{\text{obs}}-F_{\text{calc}}$ maps with extra electron density for a water molecule. The refinement of the second, stable E•S complex with 3-HAA, showed no excess residual density. To ensure that no oxygen species are present in these two structures, we also attempted to model dioxygen adjacent to the 3-HAA and the Fe(II) in the structures. The results revealed negative $F_{\text{obs}}-F_{\text{calc}}$ electron density at the site that superimposed with the dioxygen molecule, while the electron density on 3-HAA was undisturbed. In (E•S)_I, residues from loop A and B in the open conformation fit the electron density well, while residues from loop C fit well with closed conformation. And the refinement of the fully closed loop conformation yielded residues lacking electron density, including Pro23, Pro24, Val25, Arg27, His46, Arg47, Leu139, Lys140, Ile142, Val143, Thr144, and Pro147. In (E•S)_{II}, the loops fit well with a fully closed conformation (Figure 3D).

For the five intermediates observed beyond O₂ binding, the ligand modeling always started with 3-HAA; however, refinement suggested that none of the active sites in those structures contained 3-HAA in an unaltered form. Sequentially fitting the active site electron density features with alternative ligands that were each compatible with the proposed reaction cycle was applied by using PHENIX suite (10). The candidate ligands include 3-HAA, superoxo, alkylperoxo, epoxide-hydroxyl, ϵ -lactone-hydroxyl, and the ring-opened product, ACMS, in multiple conformations.

Each of the candidate ligands was fitted into the datasets individually. These ligands satisfied the extra electron density at the active site distinctly. As discussed in the main text, one dioxygen-incorporated species was assigned as Fe^{III}-superoxo, (E•S•O₂)_{II}. We refined this species with only 3-HAA, which resulted in both positive and negative electron densities around 3-HAA. Also, the superimposition of this superoxo structure with either the determined monodentate-bound 3-HAA or bidentate-bound 3-HAA showed differences in the orientations of the metal-ligands and 3-HAA. Furthermore, if only one oxygen atom was positioned adjacent to 3-HAA, positive density was clearly revealed, suggesting a missing oxygen atom. We further refined the data against epoxide and ϵ -lactone intermediates. However, none of the other models were able to satisfy the extra electron density at the active site (Fig. S3).

The next structure shown in the main text was assigned as an alkylperoxo intermediate, (E•S•O₂)_{III}. Likewise, we attempted to fit and refine the density with different ligands by using the same strategy as above. As shown in Fig. S5, the green positive electron density adjacent to 3-HAA suggests a missing oxygen atom or atoms in the structures. When this species was assigned to an

epoxide or ϵ -lactone intermediate, no density covered the oxygen inserted to 3-HAA. The assignment of this species to ACMS also resulted in unsatisfactory electron density; the structure of ACMS is more linear compared to 3-HAA and its derivatives before aromatic ring opening. The result indicated that there was not enough room to accommodate ACMS in both Fe-bound superoxo and alkylperoxo intermediates.

The structure of 1.59 Å resolution shown in the main text was assigned as a lactone radical intermediate, $(E\bullet Int)_{II}$. The electron density showed a large non-planar ring, which was unable to accommodate any 3-HAA based intermediate. The first non-planar ring candidate, an epoxide species, did not fit the electron density as well as the lactone intermediate (Fig. S6). Two resonance structures of neutral and radical-based ϵ -lactone, in $(E\bullet Int)_{II}$ and $(E\bullet Int)_{III}$, had distinct torsion and bond length, which enabled us to exclude the $(E\bullet Int)_{III}$. The C3 carbon of lactone and iron showed some negative density, presumably due to the radical character and the electron transfer between resonance structures. Fitting to the ACMS enol tautomer of $3E,5Z,2t,4c$ conformation yielded negative electron density around the newly generated carboxyl group and positive electron density at the position of C2-C3 after bond cleavage, suggesting an incorrect assignment.

The first dioxygenated product structure was assigned as a monodentate ACMS structure at a 2.10 Å resolution. As shown in Fig. S8, the extra electron density at the active site cannot be covered either by 3-HAA, superoxo, alkylperoxo, epoxide, or the ϵ -lactone. Only the ring-opened product, ACMS, had a reasonable fit. The torsion angles of the ACMS ligand require the assignment of the C2-C3 and C4-C5 bonds as single, and the trending of electron density maps indicates a $2t,4c$ conformation; thus, we modeled the enol tautomer of ACMS. The keto tautomers of ACMS could not satisfy the density maps. The strong density resulting from both carboxyl groups enabled an unambiguous assignment as the $3E,5Z$ conformation. The electron density of iron coordination only accommodated one oxygen atom of the newly formed carboxyl, and bidentate coordination resulted in strong negative density maps around the iron center. Hence, this structure was identified as a monodentate ligand of $3E,5Z,2t,4c$ -enol tautomer of ACMS.

The second product-bound intermediate structure refined to 1.84 Å resolution was obtained with slightly longer incubation time. Likewise, the broken electron density of the substrate aromatic ring was not satisfied with fitting either ring-based models, including 3-HAA, superoxo, epoxide, alkylperoxo, or the ϵ -lactone (Fig. S9). However, in this dataset, a strong electron density was found around iron coordination, which was sufficient to accommodate a bidentately bound carboxyl group. The monodentate product was no longer fitted to the electron density in this case, while a bidentate ligand of enol tautomer resulted in a satisfying fitting. Subsequent fitting with either $2t,4c$ or $2t,4t$ conformation resulted in positive densities around the enol group. Upon fitting with both conformations, the extra positive electron density was resolved. Hence, this structure contains two enol tautomers of ACMS. Keto tautomers of ACMS could not satisfy the density maps. The distance between oxygen atom on C6 and the side chain of Glu110 is 3.0 Å (Figure 5A). Such a short distance indicates a strong hydrogen bond, which could be achieved in the protonated enol, not the deprotonated keto form of ACMS. The refined occupancy was finalized as 0.45 and 0.35 for $(E\bullet P)_I$ and $(E\bullet P)_{II}$, respectively.

Structure validation and reproducibility—At each of the time points, separate crystals were prepared and analyzed. Among the crystal structures determined at each time point, the best-fit structure was chosen to represent the corresponding intermediate based on the following criteria:

1) the positions of the carbon atoms are at the center of the electron density, 2) the occupancy and B-factors for each of the intermediates are linked by model refinement; each atom in the refined structure must not exhibit drastically different refinement statistics compared to that of the surrounding residues, 3) the bond-lengths and angles are consistent with the predicted intermediates, 4) the completeness is greater than 98%, and the ligand occupancy is greater than 80%, and 5) the interactions between the ligand and the surrounding residues produces no clashes. The implementation of these criteria enabled us to rule out the overlapping structures and pinpoint the time points necessary for trapping distinctive reaction cycle intermediates.

Table S1. X-ray crystallography data collection and refinement statistics¹

Data collections	Resting state	(E•S) _I monodentate	(E•S•O ₂) _{I,II} superoxo	(E•S•O ₂) _{III} alkylperoxo	(E•Int) _{II} lactone	(E•P) _I (ACMS) _I ²	(E•P) _{I,II} (ACMS) _{I,II} ²
Beamline	SSRL Station 9-2	APS Sector 19-BM	APS Sector 19-BM	APS Sector 19-BM	APS Sector 19-ID	APS Sector 22-BM	APS Sector 19-ID
Wavelength (Å)	1.0000	0.97919	0.97919	0.97919	0.97918	1.0000	0.97918
Resolution	50.00 - 1.60 (1.63 - 1.60) ^a	50.00 - 1.90 (1.93 - 1.90)	50.00 - 1.95 (1.98 - 1.95)	50.00 - 2.30 (2.34 - 2.30)	50.00 - 1.59 (1.62 - 1.59)	50.00 - 2.10 (2.14 - 2.10)	50.00 - 1.84 (1.87 - 1.84)
Space group	<i>P</i> 6 ₅ 22	<i>P</i> 6 ₅ 22	<i>P</i> 6 ₅ 22	<i>P</i> 6 ₅ 22	<i>P</i> 6 ₅ 22	<i>P</i> 6 ₅ 22	<i>P</i> 6 ₅ 22
Cell dimensions							
<i>a</i> , <i>b</i> , <i>c</i> (Å)	57.9, 57.9, 231.4	58.0, 58.0, 231.9	58.0, 58.0, 231.3	57.8, 57.8, 231.4	58.5, 58.5, 231.9	58.6, 58.6, 231.8	58.3, 58.3, 232.0
α , β , γ (°)	90, 90, 120	90, 90, 120	90, 90, 120	90, 90, 120	90, 90, 120	90, 90, 120	90, 90, 120
Total reflections	627533	365092	365881	183975	1009118	401957	788526
Unique reflections	31413	19246	17991	11036	32318	14606	21430
Multiplicity	20.0 (14.8)	19.0 (19.7)	20.3 (21.2)	16.7 (17.4)	31.2 (33.1)	27.5 (15.9)	36.8 (37.8)
Completeness (%)	99.3 (99.9)	99.7 (100.0)	99.9 (100.0)	99.6 (100.0)	98.2 (100.0)	98.5 (96.4)	99.6 (100.0)
Mean <i>I</i> / σ (<i>I</i>)	33.6 (2.3)	39.6 (3.8)	39.9 (4.0)	27.24 (3.1)	48.2 (3.1)	33.1 (2.1)	31.25 (4.8)
<i>R</i> _{merge} ^b (%)	9.9 (90.1)	8.6 (89.6)	9.0 (94.1)	12.2 (99.6)	8.3 (82.1)	10.7 (64.9)	14.3 (93.5)
CC _{1/2}	0.997(0.982)	0.999(0.978)	1.000(0.965)	0.998(0.982)	0.999(0.991)	0.999(0.931)	0.997(0.983)
Refinement							
Resolution	46.03 - 1.60	29.00 - 1.90	29.02 - 1.95	30.06 - 2.31	30.73 - 1.59	38.20 - 2.10	42.29 - 1.84
No. of reflections; refinement	24998	19143	17907	9921	32017	14481	21334
<i>R</i> _{work} ^c / <i>R</i> _{free} ^d (%)	19.87/22.91	19.85/25.43	20.84/26.26	22.52/27.52	20.44/24.62	21.89/27.93	20.12/24.46
B-factors (Å ²)/No. of atoms							
Protein	21.7/1439	33.0/1409	21.1/1438	30.6/1388	40.5/1438	35.2/1414	31.7/1447
Iron	21.8/2	34.8/2	24.2/2	36.7/2	38.0/2	36.6/2	34.5/2

3-HAA or intermediate	N/A	35.0/11	24.0/13	36.4/13	42.5/13	40.6/13	29.2/18
Solvent	38.5/306	43.1/170	27.7/189	32.9/105	53.0/186	38.5/113	39.3/174
Root-mean-square deviation							
Bond lengths (Å)	0.007	0.015	0.008	0.016	0.014	0.014	0.020
Bond angles (°)	0.934	1.410	1.030	1.021	1.334	1.414	1.680
Ramachandran statistics							
Favored (%)	97.74	97.09	97.71	95.21	97.71	96.51	97.19
Allowed (%)	2.26	2.91	1.72	4.14	2.29	2.91	2.25
Outliers (%)	0.00	0.00	0.57	0.00	0.00	0.58	0.56
PDB entry ID	6VI5	6VI6	6VI8	6VI9	6VIA	6X11	6VIB

¹ The dataset **6VI7**.pdb for (E•S)_{II} (DOI: 10.2210/pdb6VI7/pdb) is nearly identical to the previously published 1YFY.pdb, albeit the new structure was solved at a better resolution (2.61 vs. 3.20 Å resolution).

² (ACMS)_I: 3E,5Z,2t,4c-enol tautomer of ACMS, and (ACMS)_{II}: 3E,5Z,2t,4t-enol tautomer of ACMS.

^a Values in parentheses are for the highest resolution shell.

^b $R_{\text{merge}} = \sum_i |I_{\text{hkl},i} - \langle I_{\text{hkl}} \rangle| / \sum_{\text{hkl}} \sum_i I_{\text{hkl},i}$, where $I_{\text{hkl},i}$ is the observed intensity and $\langle I_{\text{hkl}} \rangle$ is the average intensity of multiple measurements.

^c $R_{\text{work}} = \sum ||F_o| - |F_c|| / \sum |F_o|$, where $|F_o|$ is the observed structure factor amplitude, and $|F_c|$ is the calculated structure factor amplitude.

^d R_{free} is the R factor based on 10% of the data excluded from refinement.

Table S2. Coordination distances between exogenous ligands and iron before O₂ activation. Structures include enzyme alone (6VI5), 3-HAA monodentate binding (6VI6), and bidentate chelation (6VI7). Carbon atoms are numbered in blue according to the initial substrate.

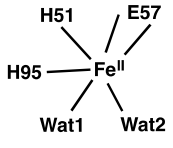
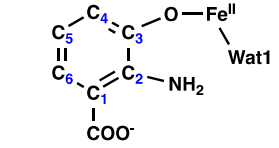
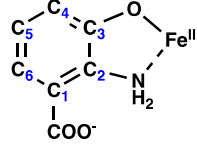
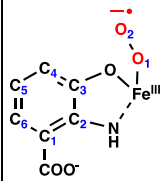
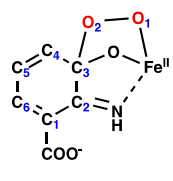
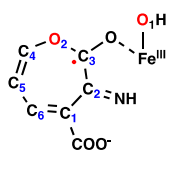
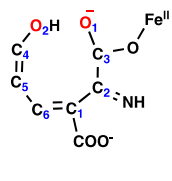
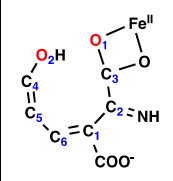
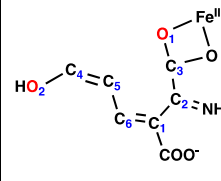
Structure and PDB entry			
	E 6VI5	(E•S) _I 6VI6	(E•S) _{II} 6VI7
Distance (Å)			
Fe – Wat1	2.1	2.5	N/A
Fe – Wat2	2.0	N/A	N/A
Fe – O _{3-HAA}	N/A	2.3	2.0
Fe – N _{3-HAA}	N/A	3.2	2.3

Table S3. Coordination distances between exogenous ligands and iron after O₂ activation. Structures include superoxo (6VI8), alkylperoxo (6VI9), ε-lactone (6VIA), monodentate enol tautomer of 3*E*,5*Z*,2*t*,4*c*-ACMS (6X11), and bidentate enol tautomers of 3*E*,5*Z*,2*t*,4*c*- and 3*E*,5*Z*,2*t*,4*t*-ACMS (6VIB, two conformations in one crystal structure). Oxygen atoms from dioxygen are colored in red. Carbon atoms are numbered according to the initial substrate.

Structure and PDB entry						
Distance (Å)	(E•S•O ₂) _{I, II} 6VI8	(E•S•O ₂) _{III} 6VI9	(E•Int) _{II, III} 6VIA	(E•P) _I 6X11	(E•P) _I 6VIB	(E•P) _{II} 6VIB
Fe – O ₁	2.1	2.3	2.2	4.0	2.2	
Fe – O ₂	3.1	2.8	4.5	5.8	4.7	6.8
Fe – O _{3-HAA}	2.3	2.5	2.3	2.4	2.3	
Fe – N _{3-HAA}	3.3	3.0	3.7	3.4	3.8	
O ₁ – O ₂	1.4	1.2	4.4	3.4	2.7	4.8
C ₃ – O ₂	3.1	1.8	1.4	3.1	2.9	4.7

Table S4. Occupancies of exogenous ligands after oxygen activation. Structures include Fe-bound superoxo (6VI8), alkylperoxo (6VI9), ϵ -lactone (6VIA), monodentate 3*E*,5*Z*,2*t*,4*c*-enol tautomer of ACMS (6X11), and bidentate 3*E*,5*Z*,2*t*,4*c*- and 3*E*,5*Z*,2*t*,4*t*-enol/ enamine tautomers of ACMS (6VIB, two conformations in one crystal structure). Oxygen atoms from dioxygen are colored in red. Carbon atoms are numbered according to the initial substrate.

Structure and PDB entry						
Occupancy						
Atom	(E•S•O ₂) _{I,II} 6VI8	(E•S•O ₂) _{III} 6VI9	(E•Int) _{I,III} 6VIA	(E•P) _I 6X11	(E•P) _I	(E•P) _{II}
Fe	1.00	1.00	0.80	1.00	0.80	
O1	1.00	1.00	0.80	1.00	0.80	
O2	1.00	1.00	0.80	1.00	0.45	0.35
C1	1.00	1.00	0.80	1.00	0.45	0.35
C2	1.00	1.00	0.80	1.00	0.80	
C3	1.00	1.00	0.80	1.00	0.80	
C4	1.00	1.00	0.80	1.00	0.45	0.35
C5	1.00	1.00	0.80	1.00	0.45	0.35
C6	1.00	1.00	0.80	1.00	0.45	0.35
N	1.00	1.00	0.80	1.00	0.80	
O	1.00	1.00	0.80	1.00	0.80	

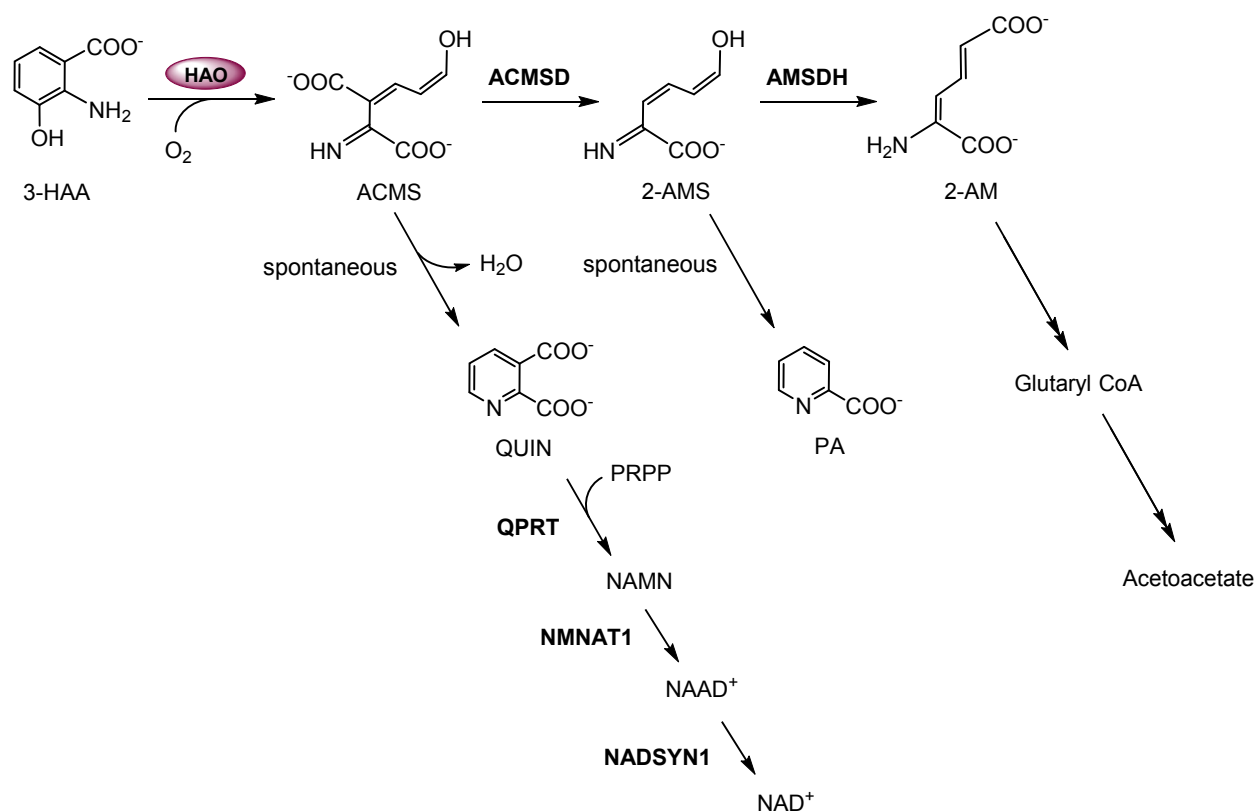
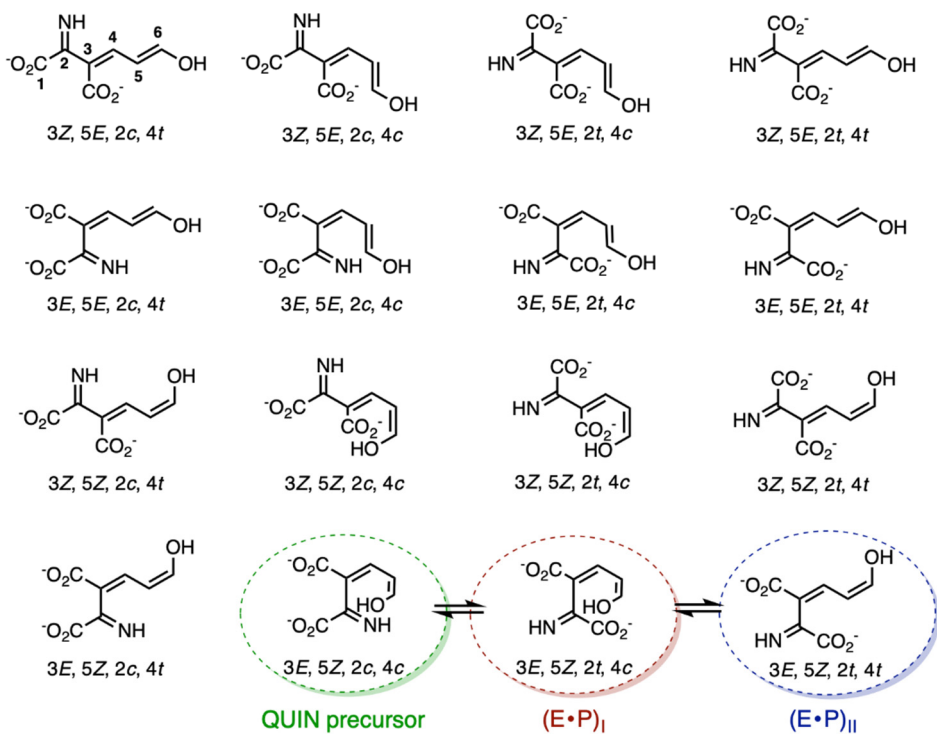


Fig. S1. The fate of the HAO reaction product, ACMS, and biosynthesis of NAD⁺. The abbreviations used for metabolites in this figure are as follows: ACMS, 2-amino-3-carboxymuconate-6-semialdehyde; 2-AM, 2-aminomuconate; 2-AMS, 2-aminomuconate-6-semialdehyde; 3-HAA, 3-hydroxyanthranilic acid; NAAD⁺, nicotinic acid adenine dinucleotide; NAMN, nicotinic acid mononucleotide; NAD⁺, nicotinamide adenine dinucleotide; PA, picolinic acid; PRPP, phosphoribosyl pyrophosphate, and QUIN, quinolinate. The abbreviations used for enzymes are as follows: ACMSD, 2-amino-3-carboxymuconate-6-semialdehyde decarboxylase; AMSDH, 2-aminomuconate-6-semialdehyde dehydrogenase; HAO, 3-hydroxyanthranilic acid dioxygenase; NADSYN1, glutamine-dependent NAD⁺ synthetase; NMNAT, nicotinamide nucleotide adenylyltransferase; and QPRT, quinolinate phosphoribosyltransferase.

Enol tautomers:



Keto tautomers:

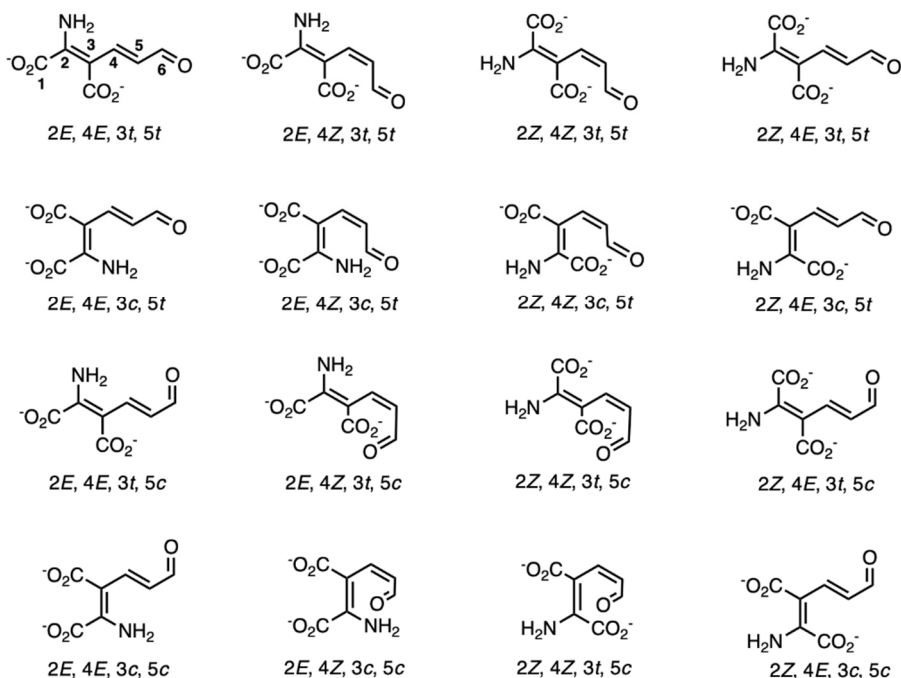


Fig. S2. Proposed thirty-two possible enol and enamine conformations of ACMS. The conformations discussed in the text corresponding to quinolinic acid (QUIN) precursor, (E•P)_I, and (E•P)_{II} are highlighted in green, red, and blue circles, respectively.

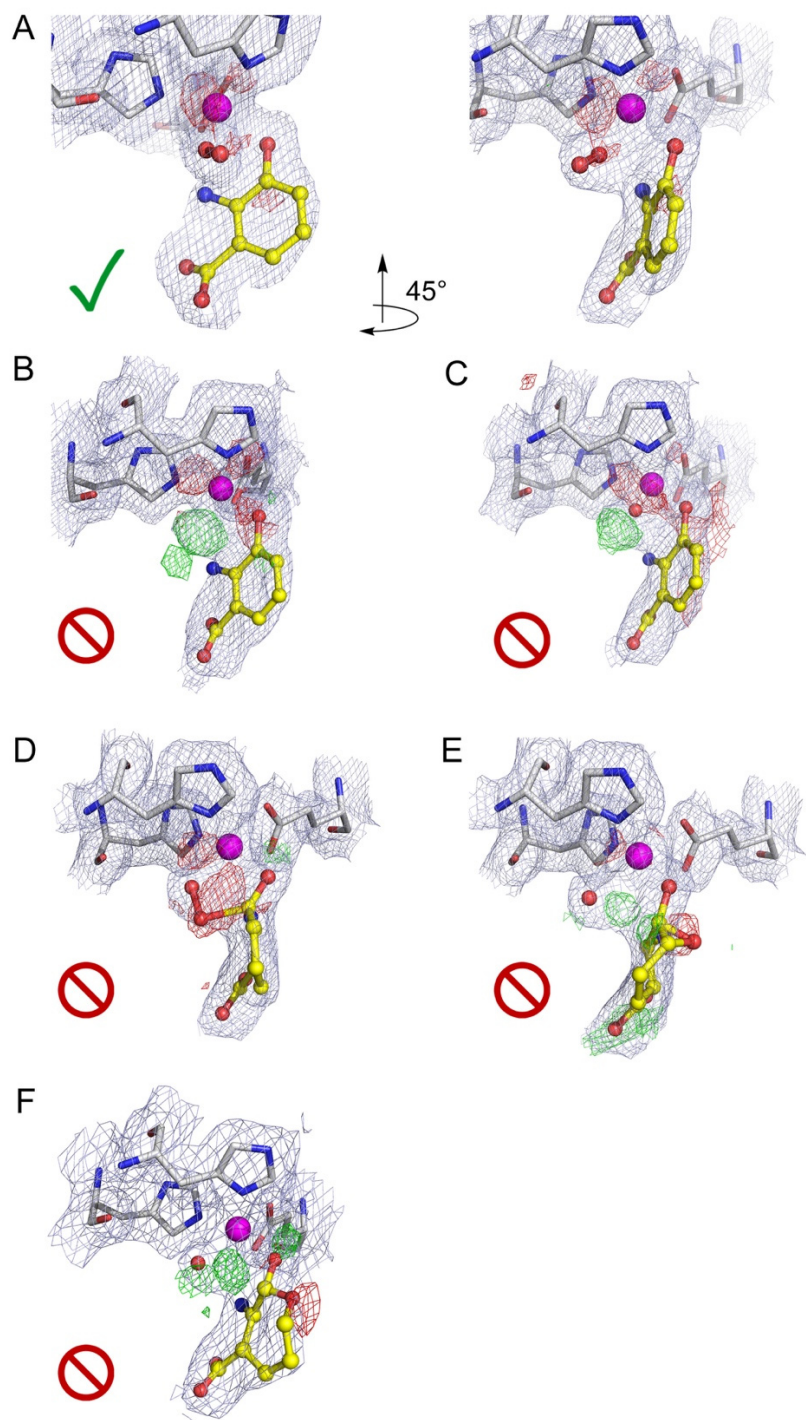


Fig. S3. Density maps for the superoxo intermediate refined using different models.

A) superoxo, B) 3-HAA, C) 3-HAA with one oxygen atom modeled at the adjacent side, D) alkylperoxo, E) epoxide with an Fe-bound hydroxyl, and F) ϵ -lactone with an Fe-bound hydroxyl. The light blue $2F_{\text{obs}} - F_{\text{calc}}$ maps are contoured at 1.0σ . The $F_{\text{obs}} - F_{\text{calc}}$ electron density maps are contoured at 3.0σ and -3.0σ in green and red, respectively. Product ACMS with different forms were not considered since the ligand electron density is in a ring-based shape. Green checks represent a suitable fitting, and slashed red circles represent improper fitting.

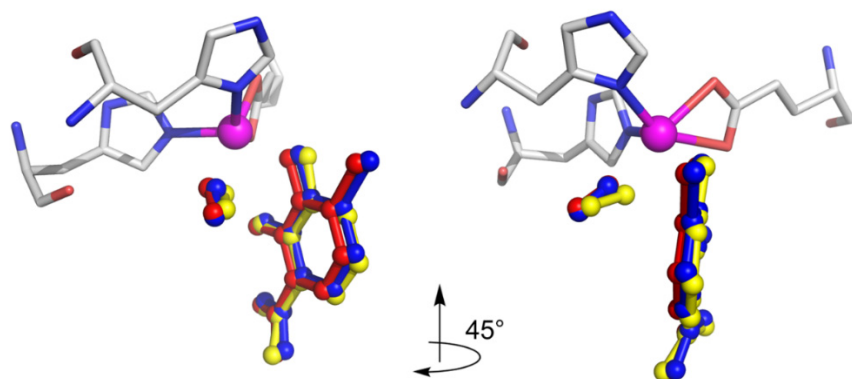


Fig. S4. Alignment of the captured superoxo with the published analogue structures.
Yellow, superoxo intermediate reported in this work; blue, superoxo intermediate of the inhibitor-bound HAO ternary complex (1YFW.pdb); and red, the NO-bound ternary complex (1YFX.pdb).

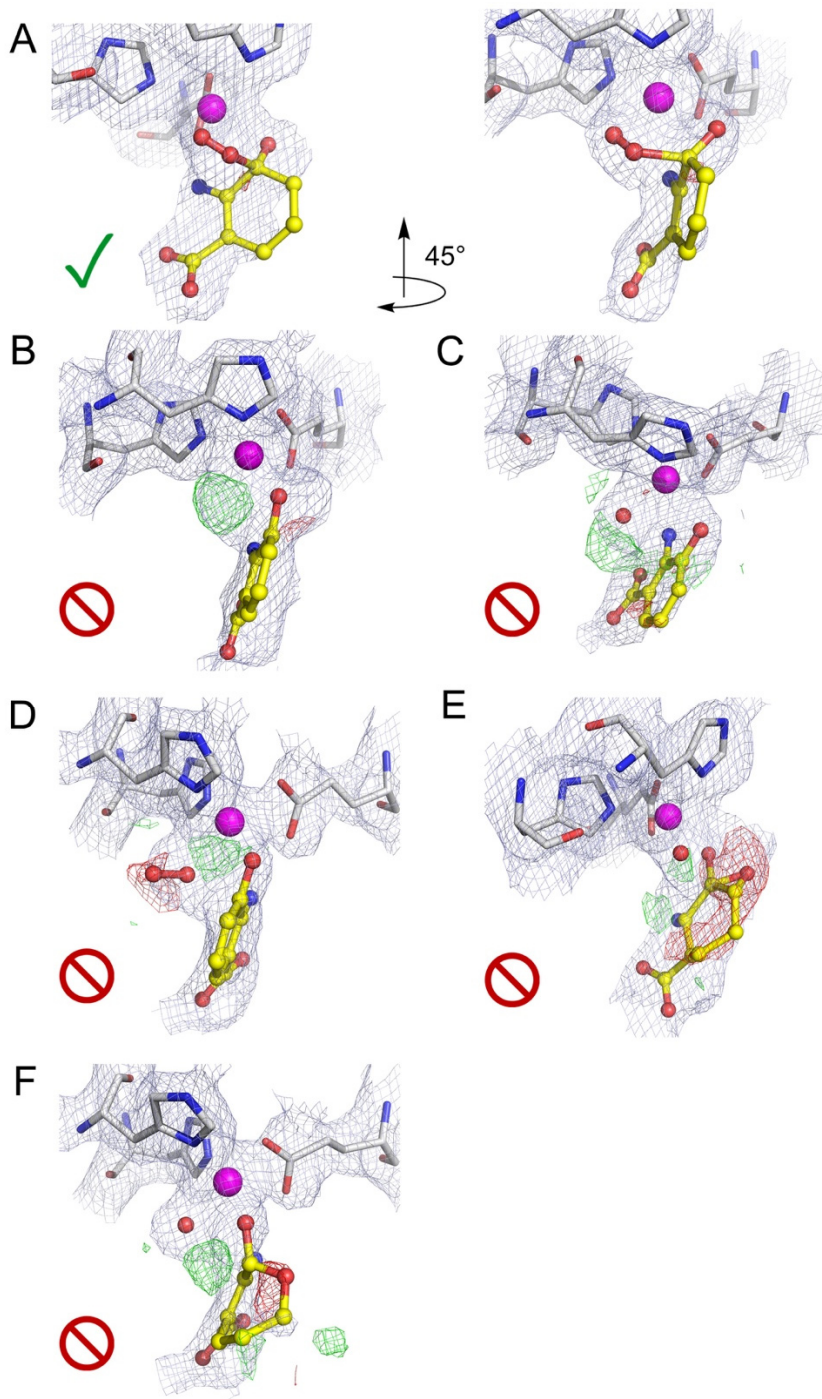


Fig. S5. Density maps for the alkylperoxy intermediate refined using various models.

A) alkylperoxy, B) 3-HAA, C) 3-HAA with one oxygen atom modeled at the adjacent side, D), superoxo, E) epoxide with an Fe-bound hydroxyl, and F) ϵ -lactone with an Fe-bound hydroxyl. The light blue $2F_{\text{obs}} - F_{\text{calc}}$ maps are contoured at 1.0σ . The $F_{\text{obs}} - F_{\text{calc}}$ density maps are contoured at 3.0σ and -3.0σ in green and red, respectively. ACMS in linear forms were not considered since the ligand density exhibits a ring structure. The green check represents a suitable fitting, and slashed red circles represent improper fitting.

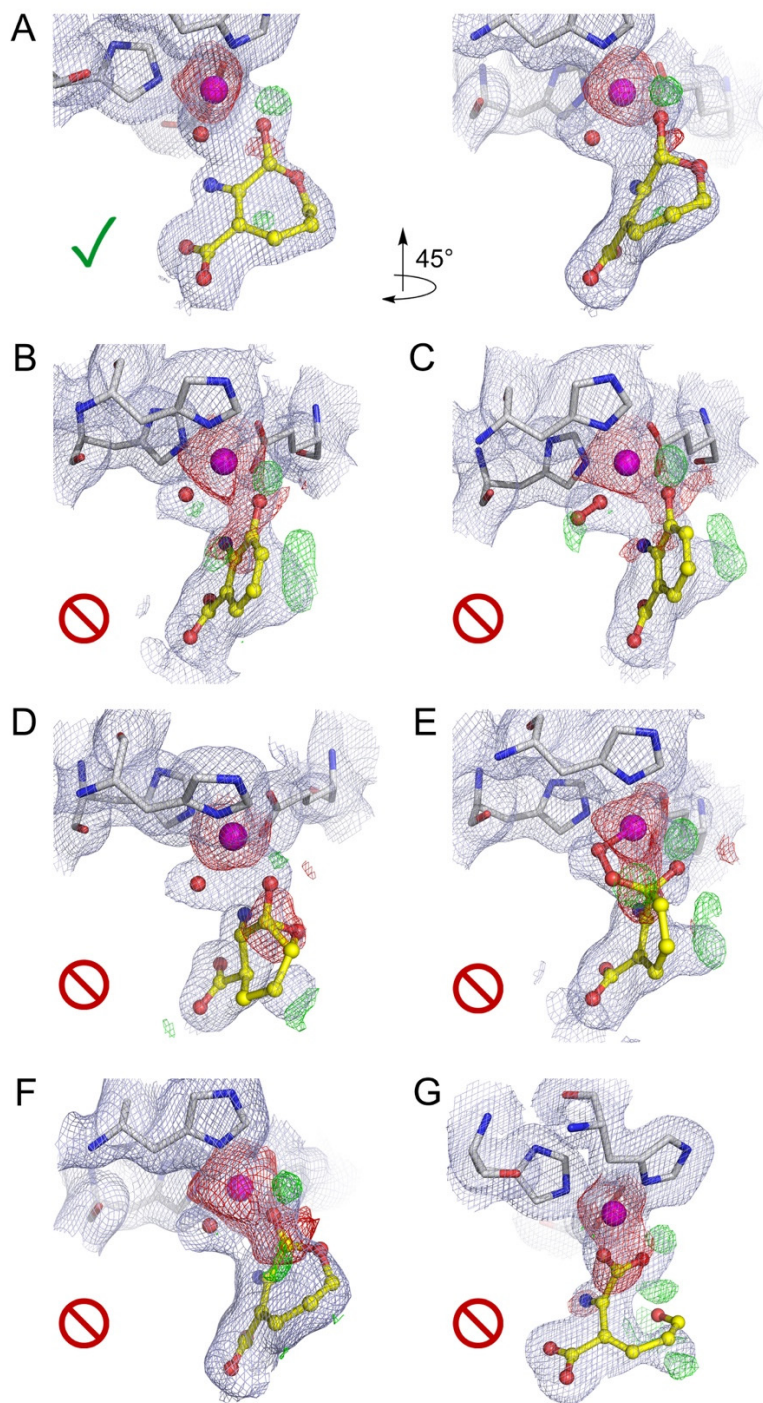


Fig. S6. Density maps for the ϵ -lactone intermediate refined using various models.

A) ϵ -lactone radical with a ferric-bound hydroxyl ($E \cdot \text{Int}_{\text{II}}$), B) 3-HAA with one oxygen atom modeled at the adjacent side, C) superoxo, D) epoxide with an Fe-bound hydroxyl, E) alkylperoxo, F) neutral ϵ -lactone with a ferrous-bound hydroxyl ($E \cdot \text{Int}_{\text{III}}$), and G) 3*E*,5*Z*,2*t*,4*c*-enol tautomer of ACMS. The light blue $2F_{\text{obs}} - F_{\text{calc}}$ maps are contoured at 1.0σ . The $F_{\text{obs}} - F_{\text{calc}}$ density maps are contoured at 3.0σ and -3.0σ in green and red, respectively. The green check represents a suitable fitting, and slashed red circles represent improper fitting.

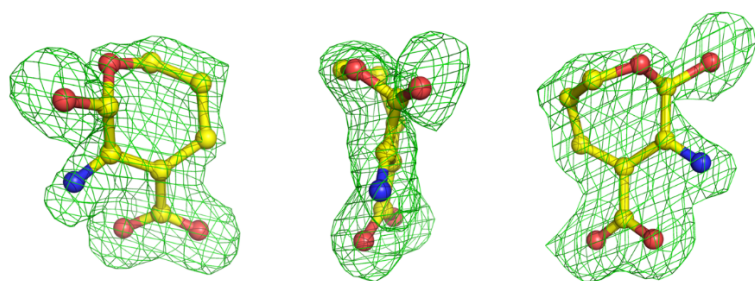


Fig. S7. Additional views of the ϵ -lactone intermediate.
The green $F_{\text{obs}} - F_{\text{calc}}$ omit maps are contoured at 3.0σ .

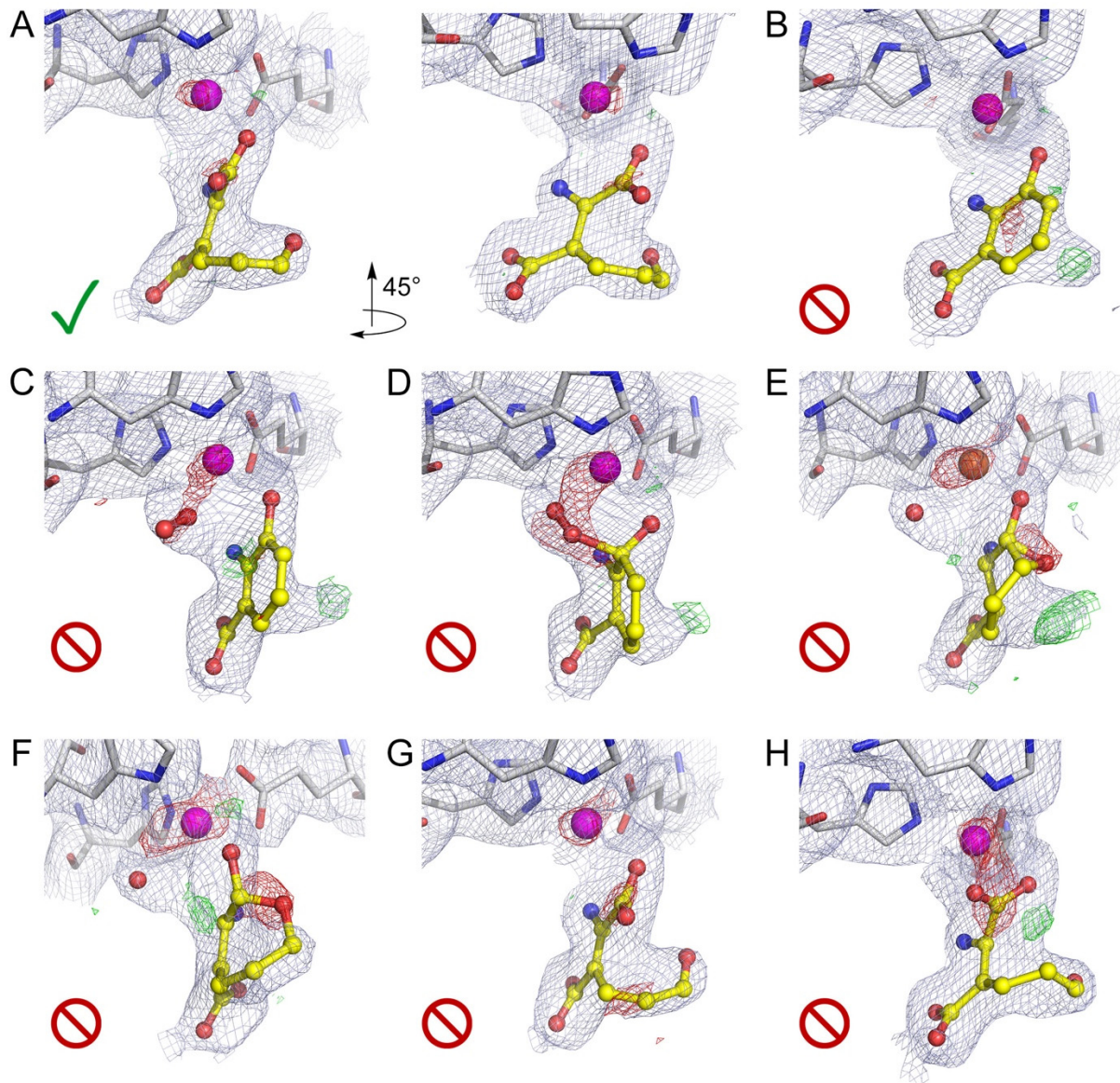


Fig. S8. Density maps for the monodentate product complex refined using various models. A) *3E,5Z,2t,4c*-enol tautomer of ACMS bound in a monodentate fashion, B) 3-HAA, C) superoxo, D) alkylperoxo, E), epoxide F) ϵ -lactone, G) keto tautomer of ACMS, and H) bidentate *3E,5Z,2t,4c*-enol tautomer of ACMS. The light blue $2F_{\text{obs}} - F_{\text{calc}}$ maps are contoured at 1.0σ . The $F_{\text{obs}} - F_{\text{calc}}$ density maps are contoured at 3.0σ and -3.0σ in green and red, respectively. The green check represents a suitable fitting, and slashed red circles represent improper fitting.

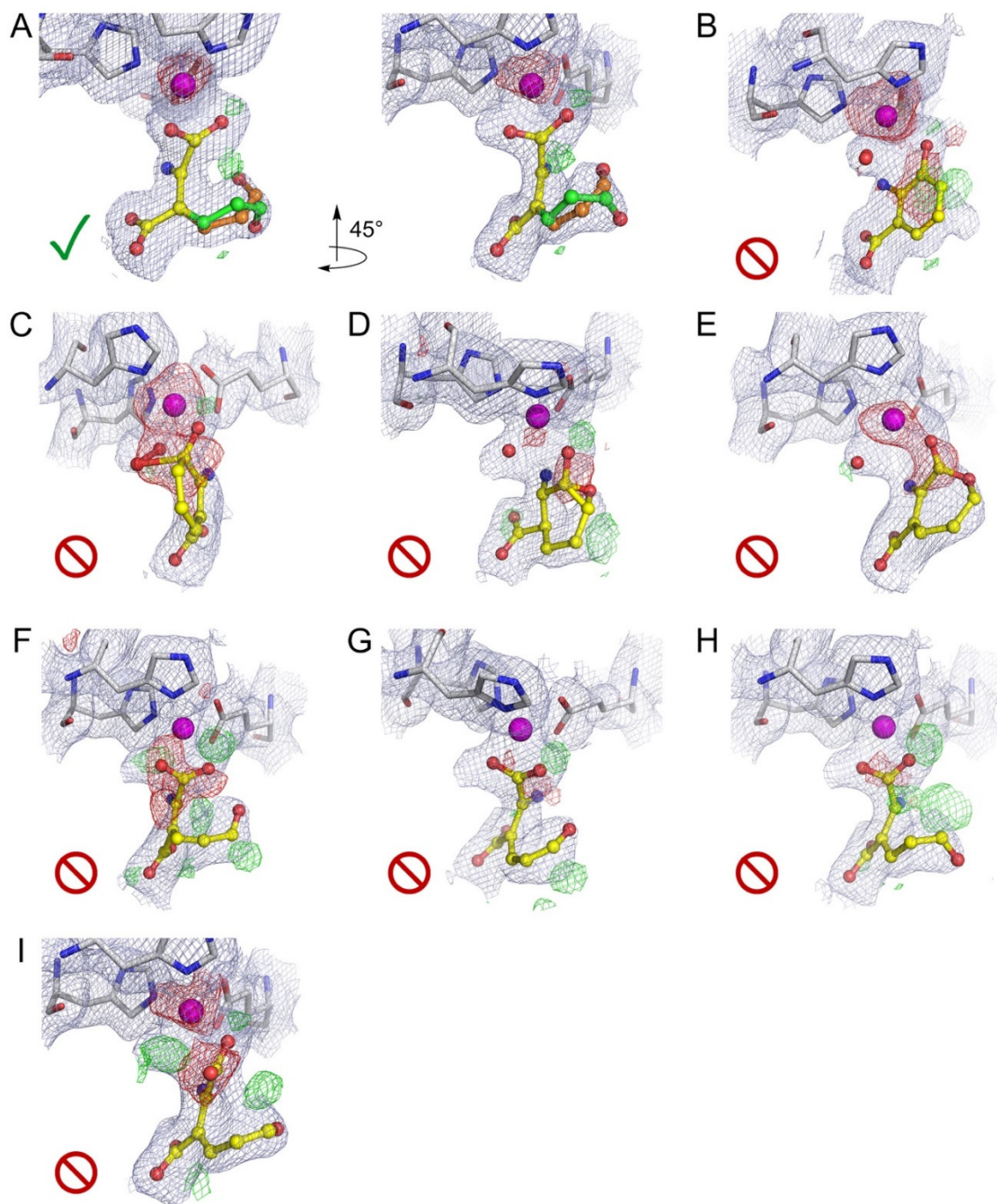


Fig. S9. Density maps for the bidentate product refined using various models. A) $3E,5Z,2t,4c$ - and $3E,5Z,2t,4t$ -enol tautomers of ACMS with an occupancy ratio of 9:7, B) superoxo, C) alkylperoxo, D) epoxide, E) ϵ -lactone, F) keto tautomer of ACMS, G) bidentate $(E \bullet P)_I$, $3E,5Z,2t,4c$ -enol tautomer, H) $(E \bullet P)_{II}$, $3E,5Z,2t,4t$ -enol tautomer, and I) monodentate $(E \bullet P)_I$. The light blue $2F_{obs} - F_{calc}$ maps are contoured at 1.0σ . The $F_{obs} - F_{calc}$ density maps are contoured at 3.0σ and -3.0σ in green and red, respectively. The green check represents a suitable fitting, and slashed red circles represent improper fitting.

References

1. T. D. Goddard *et al.*, UCSF ChimeraX: Meeting modern challenges in visualization and analysis. *Protein. Sci.* **27**, 14-25 (2018).
2. F. Liu *et al.*, An iron reservoir to the catalytic metal: The ruberoxin iron in an extradiol dioxygenase. *J. Biol. Chem.* **290**, 15621-15634 (2015).
3. Y. Yang, F. Liu, A. Liu, Adapting to oxygen: 3-Hydroxyanthranilate 3,4-dioxygenase employs loop dynamics to accommodate two substrates with disparate polarities. *J. Biol. Chem.* **293**, 10415-10424 (2018).
4. L. M. Dassama *et al.*, O₂-evolving chlorite dismutase as a tool for studying O₂-utilizing enzymes. *Biochemistry* **51**, 1607-1616 (2012).
5. Y. Zhang, K. L. Colabroy, T. P. Begley, S. E. Ealick, Structural studies on 3-hydroxy-anthranilate-3,4-dioxygenase: The catalytic mechanism of a complex oxidation involved in NAD biosynthesis. *Biochemistry* **44**, 7632-7643 (2005).
6. J. Geng, K. Dornevil, A. Liu, Chemical rescue of the distal histidine mutants of tryptophan 2,3-dioxygenase. *J. Am. Chem. Soc.* **134**, 12209-12218 (2012).
7. Y. Wang *et al.*, Biocatalytic carbon-hydrogen and carbon-fluorine bond cleavage through hydroxylation promoted by a histidyl-ligated heme enzyme. *ACS Catal.* **9**, 4764-4776 (2019).
8. Z. Otwinowski, W. Minor, Processing of X-ray diffraction data collected in oscillation mode. *Method Enzymol.* **276**, 307-326 (1997).
9. M. Strong *et al.*, Toward the structural genomics of complexes: Crystal structure of a PE/PPE protein complex from *Mycobacterium tuberculosis*. *Proc. Natl. Acad. Sci. U. S. A.* **103**, 8060-8065 (2006).
10. P. D. Adams *et al.*, PHENIX: a comprehensive Python-based system for macromolecular structure solution. *Acta Crystallogr. D Biol. Crystallogr.* **66**, 213-221 (2010).